2D Materials

Layer-selective spin-orbit coupling and strong correlation in bilayer graphene

To cite this article: Anna M Seiler *et al* 2025 *2D Mater.* **12** 035009

IOP Publishing 2D Mater. 12 (2025) 035009 https://doi.org/10.1088/2053-1583/add74a

2D Materials

OPEN ACCESS

RECEIVED
30 January 2025

REVISED
24 April 2025

ACCEPTED FOR PUBLICATION
12 May 2025

PUBLISHED
28 May 2025

PAPER

Layer-selective spin-orbit coupling and strong correlation in bilayer graphene

Anna M Seiler[1], Yaroslav Zhumagulov[2], Klaus Zollner[2], Chiho Yoon[3], David Urbaniak[1], Fabian R Geisenhof[1], Kenji Watanabe[5], Takashi Taniguchi[6], Jaroslav Fabian[2], Fan Zhang[3] and R Thomas Weitz[1,*]

[1] 1st Physical Institute, Faculty of Physics, University of Göttingen, Friedrich-Hund-Platz 1, 37077 Göttingen, Germany
[2] Institute for Theoretical Physics, University of Regensburg, 93053 Regensburg, Germany
[3] Department of Physics, University of Texas at Dallas, Richardson, TX 75080, United States of America
[4] Physics of Nanosystems, Department of Physics, Ludwig-Maximilians-Universität München, Geschwister-Scholl-Platz 1, 80539 Munich, Germany
[5] Research Center for Electronic and Optical Materials, National Institute for Materials Science, 1-1 Namiki, Tsukuba 305-0044, Japan
[6] Research Center for Materials Nanoarchitectonics, National Institute for Materials Science, 1-1 Namiki, Tsukuba 305-0044, Japan
[*] Author to whom any correspondence should be addressed.

E-mail: thomas.weitz@uni-goettingen.de

Keywords: bilayer graphene, spin-orbit coupling, correlations

Supplementary material for this article is available online

Abstract

Spin-orbit coupling (SOC) and electron-electron interaction can mutually influence each other and give rise to a plethora of intriguing phenomena in condensed matter systems. In pristine bilayer graphene (BLG), which has weak SOC, intrinsic Lifshitz transitions and concomitant van-Hove singularities lead to the emergence of many-body correlated phases. Layer-selective SOC can be proximity induced by adding a layer of tungsten diselenide (WSe_2) on its one side. By applying an electric displacement field, the system can be tuned across a spectrum wherein electronic correlation, SOC, or a combination of both dominates. Our investigations reveal an intricate phase diagram of proximity-induced SOC-selective BLG. Not only does this phase diagram include those correlated phases reminiscent of SOC-free doped BLG, but it also hosts unique SOC-induced states allowing a compelling measurement of valley *g*-factor and a correlated insulator at charge neutrality, thereby showcasing the remarkable tunability of the interplay between interaction and SOC in WSe_2 enriched BLG.

1. Main

Various distinct strongly interacting states often compete for the ground state of a disorder-free two-dimensional (2D) electron system under electron–electron interactions. Recently, the seemingly well-explored family of few-layer graphene has gained revived interest [1–10]. For example, in the simplest AB-stacked bilayer graphene (BLG), a plethora of many-body states has been revealed [2, 4, 5, 10]. Here, electric displacement field-controlled inversion symmetry breaking further flattens the bands yet making the low-density saddle points experimentally accessible. Consequently, Stoner ferromagnetic states [2, 4, 5, 10], correlated (semi-) insulating and metallic states [4, 5], and superconducting states [2] have been identified close to the field-controlled van-Hove singularities. The detailed nature and mechanisms of these states are under active investigations. For example, it has been shown that proximity-induced spin-orbit coupling (SOC) of Ising (valley-Zeeman) type allows the observation of superconducting states in a much broader parameter space [11, 12], leading to the question of whether SOC is responsible for suppressing interacting states that compete with superconductivity [13], or whether superconductivity is enhanced by SOC [12]. To date which effect (e.g. SOC, Coulomb interaction, saddle points) favors which ground state has still been an open question both from the theoretical [13] and experimental [11, 12] sides.

While previous investigations have focused on the impact of proximity-induced SOC on the superconductivity of BLG [11, 12], impacts of such a SOC on the rest of its correlated phase diagram remains unexplored. Here, we systematically disentangle the intricate interplay between electronic correlations and SOC in spin-orbit proximitized BLG, aiming to elucidate the entire phase diagram. To this end we prioritize the competition between SOC and Coulomb interaction in their impacts on those BLG ground states enriched by the displacement field-controlled saddle points yet outside of the superconducting regime.

A typical device scheme is shown in figure 1(a), where a monolayer of WSe_2 is placed below a BLG flake. The BLG/WSe_2 heterostructures are contacted by two-terminal graphite flakes and encapsulated in hexagonal boron nitride (hBN). Additional graphite top and bottom gates are incorporated to provide electrostatic control and to ensure a high device quality. Optical microscope images of the two encapsulated devices investigated in this study are displayed in figure 1(b) and supplementary figure S1.

The dual-gate structure enables independent tuning of the charge carrier density (n) and the electric displacement field (D). In such a device configuration, Ising SOC (valley-Zeeman type) [14] is expected to only be introduced to the bottom graphene layer [12, 15, 16], which can be confirmed by our band structure calculations (figure 1(c)). The proximity-induced SOC results in out-of-plane spin-valley locking of the Ising SOC (valley-Zeeman type), and relatively large (meV) spin-splitting of the low-energy bands of BLG at the K and K' points with no overall layer asymmetry [16]. Note that the influence of Rashba SOC on the low-energy band structure is minimal (see supplementary figure S2). As a result, it is neglected in the present study. At $D > 0$ and $n > 0$ (or $D < 0$ and $n < 0$), electronic states near the Fermi energy are polarized to the layer adjacent to the WSe_2 [12, 15, 16], exhibiting the proximity spin-orbit physics. Conversely, the energy bands for $D > 0$ and $n < 0$ (or $D < 0$ and $n > 0$) are only weakly affected by the presence of WSe_2 (figure 1(c)). This D-dependent spin-valley-locked, spin-split band structure has a direct consequence for the charge transport at small n and D as shown in figure 1(d), where the occupation of the high-energy spin-split conduction and valence bands, as marked with arrows, are featured by increased $\mathrm{d}G/\mathrm{d}n$ with conductance G (see supplementary figure S3 for a complete phase diagram of both devices investigated for the present study) [15]. While these transitions are more clearly resolved in the derivative map shown in figure 1(d), they are also present—albeit less prominently—in the raw conductance data (see, for example, figure 3(e) which will be discussed later). The strength of the Ising SOC λ_I can be determined directly by mapping the magnetic field dependence of particular Landau-Levels (LL), e.g. the $\nu = 3$ state, to be $\lambda_I = (1 \pm 0.1)$ meV (see methods and supplementary figure S4), which is consistent with previous results [11, 12, 15, 17, 18] and DFT calculations [14, 16].

2. Correlated phases in the vicinity of tunable van-Hove singularities

We start our analysis in the conduction band at large D fields, where, in the absence of SOC, a cascade of correlated phases was found as low-temperature ground states (figures 1–3) [5]. Since BLG is only proximitized on one side by WSe_2, we can investigate the presence and absence of SOC in the same sample, by selectively addressing the layer-polarized energy levels. We first re-investigate the conduction band without SOC ($D < 0$, $n > 0$) in both non-proximitized BLG (figures 2(a)–(c)) and in proximitized BLG when electron transport is taking place in the top layer where the effects of SOC are weak (figures 2(d)–(f)). Consistent with previous works [5, 10], three phases can be identified at large $|D|$ close to the band edge: a spin- and valley-polarized (quasi-) insulating phase (1x), a spin-polarized (quasi-) insulating phase (2x), and a fully spin- and valley-degenerate metallic phase (4x) (figures 2(a)–(f)). The (quasi-) insulating character of the 1x and 2x phases was discussed in [5]. The labels '1x,' '2x,' and '4x' reflect the different spin and valley degeneracies of the system which are determined by examining the behavior of the phase boundaries with respect to the applied out-of-plane and in-plane magnetic field ($B_\perp$ and $B_{||}$) [5, 10]. Applying a finite $B_{||}$ (figures 2(c) and (f)), which only couples to the spin degree of freedom, does not shift the phase boundary between the 1x and 2x phases, indicating similar spin polarizations of both phases. By contrast, the phase boundary between the 2x and 4x phases shifts towards higher electron densities, indicating spin polarizations in the 1x and 2x phases but not in the 4x phase. Applying $B_\perp$, which couples to the valley and out-of-plane spin degrees of freedom via the orbital and spin Zeeman effects, affects both phase boundaries (figures 2(b) and (e)), indicating a change in valley polarization between the 1x and 2x phases, i.e. we can identify the 1x phase to be valley polarized while the 2x and 4x phases are valley unpolarized. This method allows to identify the degeneracies even at $B_\perp = 0$ where no quantum Hall oscillations are present. Remarkably, these characteristics are consistent in both non-proximitized BLG (figures 2(a)–(c)) and in proximitized BLG when electron transport is taking place in the top layer where the effects of SOC are weak (figures 2(d)–(f)).

A drastically different phase diagram appears in the same parameter space ($|D|$ and n) but for the

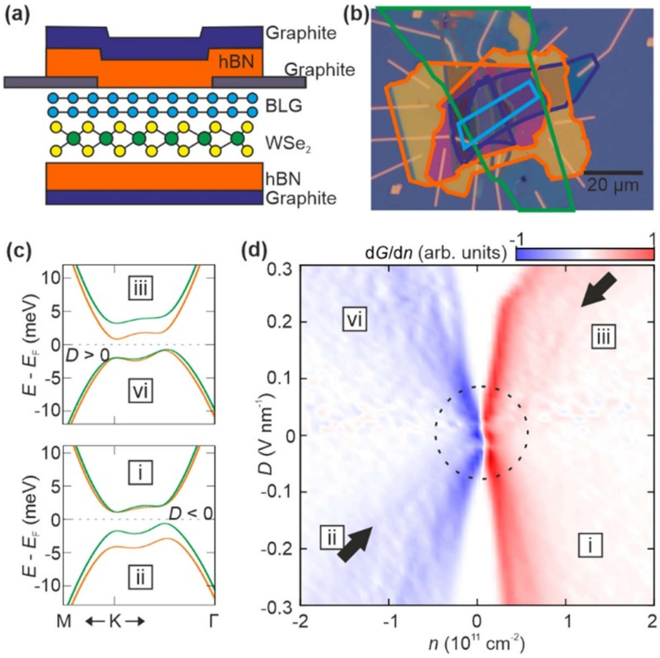

Figure 1. Phase diagram of bilayer graphene exhibiting layer-selective proximity-induced SOC. (a) Device schematic of an encapsulated bilayer graphene flake located on top of a WSe$_2$ flake. (b) Optical microscope image of Device I. Graphite flakes serving as gates (contacts) are outlined in purple (grey), hBN flakes are outlined in orange, the WSe$_2$ flake is outlined in green, and the BLG flake is outlined in blue (the same color code as in (a)). (c) Low-energy band structures of bilayer graphene near the K-point of the Brillouin zone for electric potentials $V = -2$ meV (top) and $V = 2$ meV (bottom), calculated from a model that includes an Ising SOC of $\lambda_\mathrm{I} = 1.07$ meV on the bottom layer. Green bands are spin polarized up, orange bands are spin polarized down. (d) Derivative of the two-terminal conductance G ($\mathrm{d}G/\mathrm{d}n$) as a function of charge carrier density n and electric displacement field D measured in Device I with $B_\perp = B_{||} = 0$ T at a temperature $T = 10$ mK. Changes in the conductance associated with proximity-induced spin-orbit coupling (SOC) are highlighted: the arrows indicate changes in G associated with the band splitting due to proximity-induced SOC (see figures 2(g) and 3(e) for more better visibility); the circle marks the correlated insulating state at $D = n = B_\perp = 0$, shown in more detail in figure 4. The labels i–iv mark the four quadrants in the n-D plane and correspond to the energy bands shown in **(c).**

WSe$_2$ proximitized conduction band ($D > 0$, $n > 0$, figures 2(g)–(i)). Consistent with other works [19–21], we do observe signatures of a spin/ valley polarized phase, which we attribute to the SOC-induced splitting of the originally four-fold degenerate band into two sets of two-fold degenerate spin-valley-locked bands. While the transition between the two sets of SOC-split bands shown in figure 1(d) extends to large D (figure 2(g)), in the investigated range up to 0.8 V nm, no additional conductance features indicating additional spin or valley polarization appear at $D > 0$ and $B = 0$, unlike on the non-WSe$_2$-proximitized side. It appears that in the presence of SOC, the formation of interaction-driven spin and/or valley polarized Stoner phases near the conduction band edge of D field-gapped BLG is suppressed. This picture is also consistent with the magnetic field data. Applying $\mathrm{B}_\perp$ induces a valley splitting in the low-energy spin-valley-locked band due to the valley-Zeeman effect. This splitting shifts to higher energies with increasing $B_\perp$ and manifests as a peak in $\mathrm{d}G/\mathrm{d}n$ that is marked with a dashed line in figure 2(h) and is shifting to higher n for increasing $B_\perp$. At a critical magnetic field B_C (supplementary figure S5), the upper band of the low-energy spin-valley-locked band (K valley, spin down and the lower band of the high-energy spin-valley locked band (K' valley, spin down) intersect. These bands share the same spin but have opposite valley indices. This crossing point allows us to determine the D-dependent valley g-factor, which quantifies the strength of the valley magnetic moment [22]. Using $\lambda_I = \frac{1}{2}\mu_B g_V B_C$ with Bohr magneton μ_B and $B_C = 1.9$ T, we find g_V to be 22 at $D = 0.7$ Vnm^{-1}, which aligns well with previous results obtained in BLG quantum dots [23–25]. In the $B_{||}$ map up to 2 T we do not observe any change of the phase boundaries, since in this regime the spin Zeeman energy $E_z \ll \lambda_I$ [16].

All our observations point to the weakening or absence of Stoner ferromagnetic phases when the electrons are polarized to the layer adjacent to WSe$_2$. Theoretically, the Ising SOC of out-of-plane spin quantization, together with the WSe$_2$-enhanced screening effect, is expected to disfavor those correlated phases with in-plane spin orientations as previously identified in the absence of SOC [4, 5]. We note that WSe$_2$ does have a larger dielectric constant than hBN [26]. Given that monolayer WSe$_2$ is used in our devices, the short-range part of Coulomb interaction is more significantly screened than the long-range Coulomb tail. Nevertheless,—even though the effect will likely be small—the WSe$_2$-enhanced screening

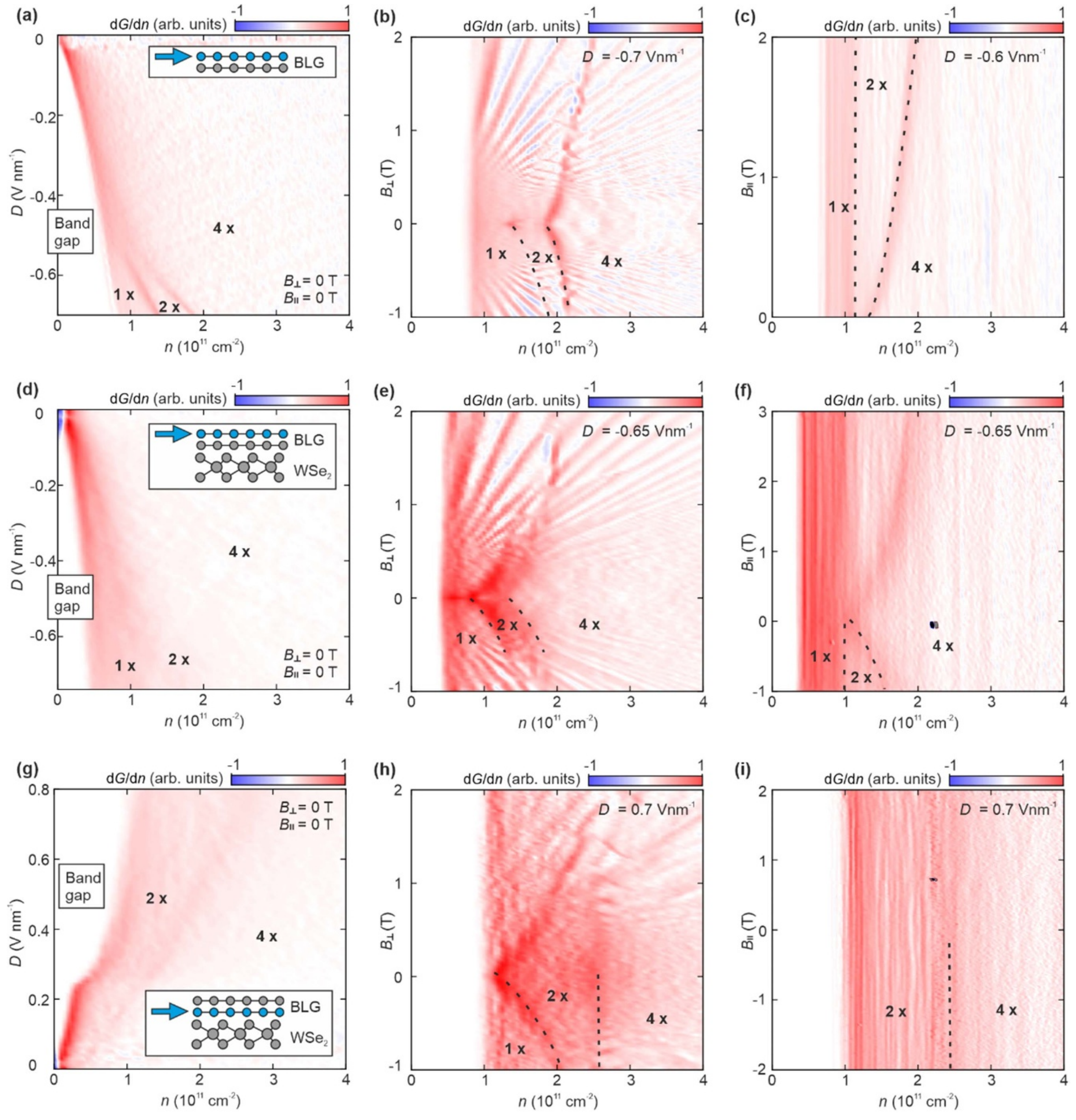

Figure 2. Phase diagrams of electron-doped bilayer graphene without and with layer-selective proximity-induced SOC. (a) dG/dn as a function of n and negative D measured in a BLG heterostructure without proximate WSe$_2$ layer (Device III) with $B_\perp = B_{||} = 0$ T. The 1x, 2x and 4x degenerate phases are labeled. (b), (c) dG/dn as a function of n and $B_\perp$ (b) and $B_{||}$ (c) for $D = -0.7$ V nm^{-1} (b) and $D = -0.6$ V nm^{-1} (c). Phase boundaries are highlighted by dashed lines. (d) dG/dn as a function of n and negative D measured in a BLG—WSe$_2$ heterostructure (Device I) with $B_\perp = B_{||} = 0$ T. Electron transport is taking place in the top layer where the effects of SOC are weak. (e), (f) dG/dn as a function of n and $B_\perp$ (e) and $B_{||}$ (f) for $D = -0.65$ V nm^{-1}. Electron transport is taking place in the top layer where the effects of SOC are weak. Phase boundaries are highlighted by dashed lines. (g) dG/dn as a function of n and positive D measured in a BLG—WSe$_2$ heterostructure (Device I) with $B_\perp = B_{||} = 0$ T. Electron transport is taking place in the bottom layer where the effects of SOC are strong. (h), (i) dG/dn as a function of n and $B_\perp$ (h) and $B_{||}$ (i) for $D = -0.65$ V nm^{-1}. Electron transport is taking place in the bottom layer where the effects of SOC are strong. Phase boundaries are highlighted by dashed lines. No changes in the phase boundaries can be observed as a function of $B_{||}$ (the n-$B_{||}$ map is dominated by vertical lines). The data presented in panels (a)–(c) was obtained using Device III, the data in panels (d)–(i) was obtained using Device I. All measurements were performed at a temperature of $T = 10$ mK.

may disfavor Stoner and more elaborate correlated phases [27–29]. The suppression of the Stoner phases on the WSe$_2$ polarized layer might be further enhanced by greater disorder at the WSe$_2$/BLG interface compared to the BLG/hBN interface (see methods for details on the sample fabrication).

The picture becomes more complex on the hole-doped side of BLG, where trigonal warping is more pronounced [30] and Lifshitz transitions with concomitant van-Hove singularities give rise to a cascade of correlated insulating and metallic phases of both Stoner and non-Stoner types [4]. These phases were initially observed in pristine BLG (see also figures 3(a), (b)) and can also be identified similarly in the BLG/WSe$_2$ devices for $D > 0$ and $n < 0$, where charge transport occurs in the layer non-adjacent to

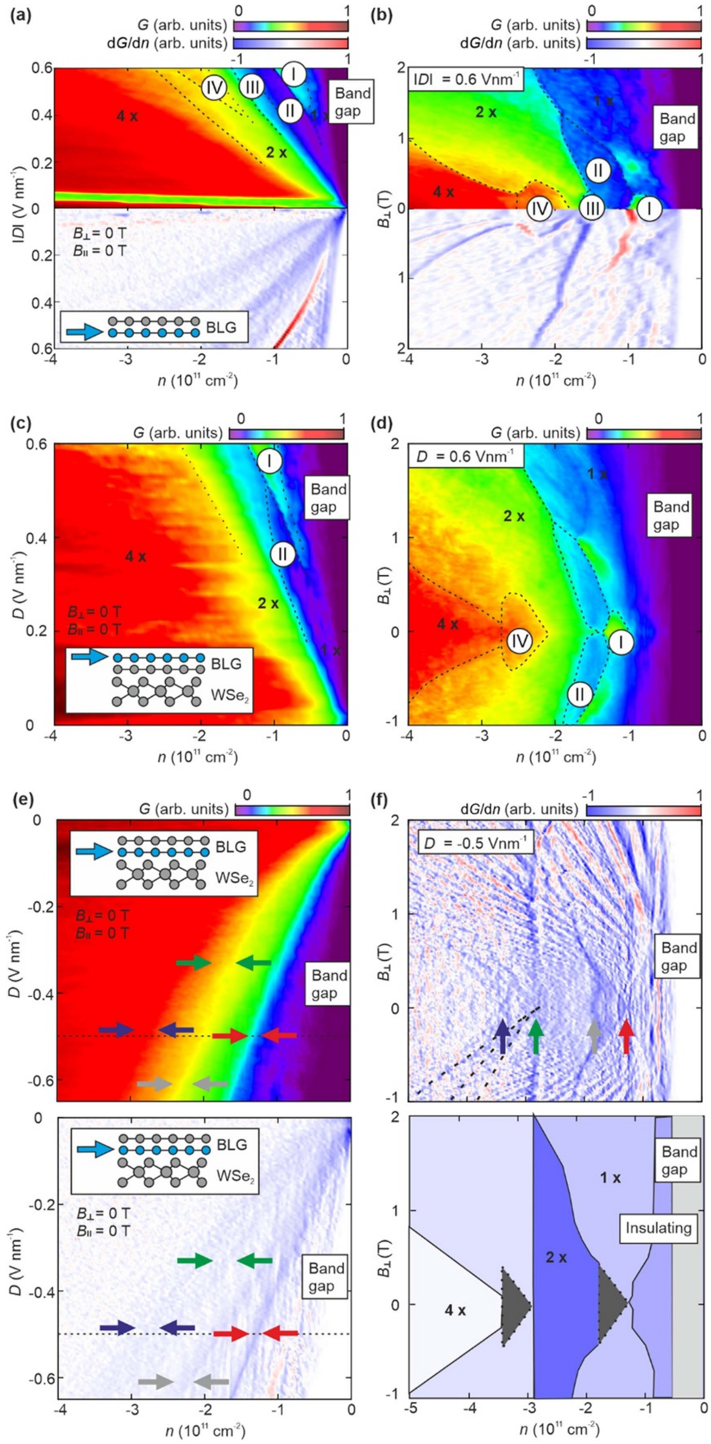

Figure 3. Phase diagrams of hole-doped bilayer graphene without and with layer-selective proximity-induced SOC. (a) Conductance G (top panel) and derivative of the conductance dG/dn (bottom panel) as a function of the charge carrier density n and electric displacement field $|D|$ measured in a BLG heterostructure without proximate WSe$_2$ layer (Device III) with $B_\perp = B_{||} = 0$ T. Electron transport is taking place in the top layer where the effects of SOC are weak. Phase boundaries are highlighted by dashed lines. The 1x, 2x and 4x degenerate phases are labeled. Interaction-induced phases are labeled according to Seiler *et al* [4]. Where phases I and IV correspond to correlated metals of non-Stoner type and phases II and III correspond to correlated insulating phases consistent with a Wigner-Hall crystal (phase II) and a trivial Wigner crystal (phase III). (b) G (top panel) and dG/dn (bottom panel) as a function of n and $B_\perp$ at $|D| = 0.6$ Vnm^{-1}. (c) G as a function of n and positive D measured in a BLG—WSe$_2$ heterostructure (Device II) with $B_\perp = B_{||} = 0$ T. Electron transport is taking place in the top layer where the effects of SOC are weak. Phase boundaries are highlighted by dashed lines. The interaction-induced phases are labeled. (d) G as a function of n and $B_\perp$ at $D = 0.6$ Vnm^{-1}. (e) G (top panel) and dG/dn (bottom panel) as a function of n and negative D with $B_\perp = B_{||} = 0$ T. Electron transport is taking place in the bottom layer where the effects of SOC are strong. Phase boundaries are highlighted by arrows. The interaction induced phases I–IV are not present. (f) Top panel: dG/dn as a function of n and $B_\perp$ for $D = -0.5$ V nm^{-1}. Phase boundaries are highlighted by arrows. Quantum Hall states arising from the second energy band are traced by dashed lines for negative $B_\perp$. Bottom panel: schematic of the different phases induced by SOC. The one-fold, two-fold, and four-fold degenerate phases are labeled as 1x, 2x, and 4x, respectively. Additional phases in the low-density regime of the 2x and 4x degenerate bands are shaded in gray. Furthermore, an insulating phase emerges near the band edge. The data presented in panels (a), (b) was obtained using Device III, the data in panels (c)–(f) was obtained using Device II. All measurements were performed at a temperature of $T = 10$ mK.

WSe_2 (figures 3(c) and (d)). However, the proximity-induced Ising SOC is present for $D < 0$ and $n < 0$ when charge transport occurs in the layer adjacent to WSe_2, and evidently it disfavors these correlated phases (see figures 3(e) and (f) for the data from Device II and supplementary figure S6 for data from Device I). Notably, our findings reveal multiple distinctive features in the density derivative of the conductance, as indicated by arrows in figures 3(e) and (f), which is in sharp contrast to our observations at low D fields (figure 1(d)), at electron doping (figures 2(e) and (f)), and in previous literature [13].

The first feature at lowest n near the band edge separates low and high conductance regimes (red arrows in figures 3(e) and (f)). In the low-conductance regime, the conductance sharply increases with increasing applied current I_{Bias} (supplementary figures S7(a) and (b)), indicating insulating behavior, possibly arising from disorder [31, 32], Wigner crystallization [33], or more exotic phenomena, e.g. induced by exchange interaction between the trigonal warping induced mini valleys [34–36]. A detailed analysis of this regime, however, extends beyond the scope of this present study. This regime is markedly different from that when WSe_2 is absent, where a metallic phase had been observed at the valence band edge [4].

Another marked difference is in the higher density regime, where a cascade of correlated metallic and insulating phases were found [4] in the absence of SOC, whereas in the presence of SOC no clear signs of physics beyond SOC can be identified. These features can be associated with the SOC-induced band splitting and the occupation of the second energy band (green arrow in figures 3(e) and (f)), exhibiting $B_{||}$- and $B_{\perp}$-dependences similar to those observed at the electron doped case with induced SOC (supplementary figures S8 and 3(f)).

Additional phase boundaries (blue and gray arrows in figures 3(e) and (f)) emerge within the spin-valley-locked bands, with the corresponding phases shaded gray in the lower panel of figure 3(f) [11, 12]. Since trigonal warping is more pronounced in the valence band [30], these boundaries may separate regions with a different Fermi surface topologies, i.e. where the Fermi surface transitions from being three-fold degenerate to one-fold degenerate. Alternatively, they may mark the transition from a partially isospin-polarized to a fully isospin-polarized regime. This interpretation is supported by the appearance of an additional fan with Landau levels that curve in the n-$B_{\perp}$ space (see e.g. dashed lines in figure 3(f)) and has been attributed to a partially isospin-polarized regime with small minority Fermi pockets [1, 2].

With the exception of the phase at lowest n, the prevalence of mainly SOC-driven states is also supported by the absence of non-linear $\mathrm{d}I/\mathrm{d}V$ feature and the lack of strong temperature dependence (supplementary figures S7(a)–(c)). Finally, we note the absence of any indication of superconductivity near these potential phase boundaries [11, 12]. This may be attributed to constraints imposed by the application of higher D-fields due to elevated gate currents and the use of thicker hBN dielectrics in the range of 37 nm to 62 nm compared to two previous studies [11, 12].

3. Transport in WSe_2 proximitized BLG at overall charge neutrality

While at large D fields and finite doping the correlated phases are strongly suppressed when charge carriers are layer-polarized to the WSe_2-BLG interface, the situation is different at charge neutrality when there is no layer polarization ($D = n = 0$). The ground state of undoped BLG has been intensively addressed by multiple works [7, 37–41]; the strength of Coulomb interaction plays a critical role. In the limit of strong interaction, as experimentally realized in suspended BLG, an insulating layer antiferromagnetic (LAF) state has been identified as the ground state [7, 37–41]. In the LAF state, two spin species spontaneously polarize to opposite layers [22]. On the other hand, in hBN encapsulated BLG, interaction is weaker due to the larger dielectric constant $\in_{\mathrm{r}}$ and closer distance of screening metal gates (about 150 nm in the suspended samples and typically below 60 nm in hBN encapsulated samples), and the LAF state has not been found. Thus, one may wonder whether the ground state is still correlated or non-interacting given the induced SOC but the weakened Coulomb interaction.

From our multi-scale theoretical investigation of the single-particle bands (figures 4(f) and (g)), consistent with previous reports, a SOC-split but overall gapless band structure is present. An interesting question now is whether the induced Ising SOC and the more screened interaction lead to a correlated insulating state like in the freestanding case or disfavor correlated states as in the case of large D fields discussed above. Figure 4 shows our experimental observations, and a region of suppressed conductance is evident at charge neutrality. This region is unstable against the application of doping or a D field of either sign. These suggest most likely the topologically trivial LAF state as in the freestanding case [7, 37–41], and with increasing $B_{\perp}$ the LAF state evolves into a canted antiferromagnetic (CAF) state (figure 4(c)) [42–44]. Furthermore, this state is not strongly affected by the application of a $B_{||}$ field (figure 4(d)), consistent with two previous studies [41, 44]. In addition, we observe insulating behavior, i.e. decreasing resistance with increasing temperature or increasing current (figure 4(e) and supplementary figure S9). The insulating state is stable below 5 K, and we extract an energy gap of 0.4 meV using Arrhenius

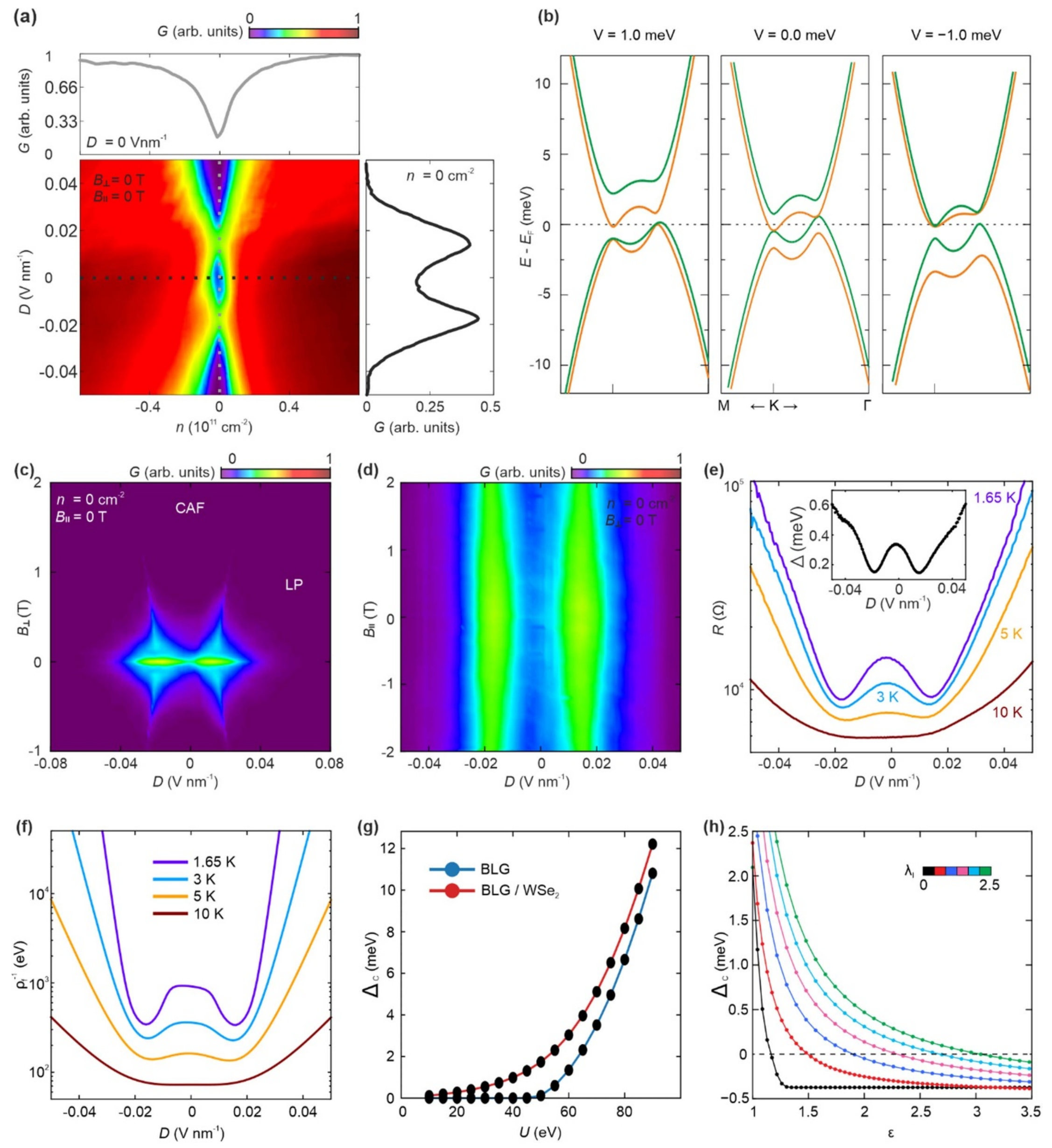

Figure 4. Correlated insulating state at $D = n = B_\perp = 0$ and multi-scale modeling. (a) Two-terminal conductance G in arbitrary units (arb. units) as a function of D and n at zero magnetic field B measured in a BLG—WSe$_2$ heterostructure (Device I) at a sample temperature of $T = 10$ mK. Line traces are shown for $D = 0$ and $n = 0$, respectively. (b) Non-interacting band structures of bilayer graphene on top of WSe$_2$ at different interlayer electric potentials. Green bands are spin polarized up, orange bands are spin polarized down. No band gap is open at $V = 0$. (**c**) G as a function of D and an out-of-plane magnetic field $B_\perp$ at $n = 0$ and $T = 10$ mK. The layer antiferromagnetic (LAF), canted antiferromagnetic (CAF) and layer polarized (LP) states are labeled. (**d**) G as a function of D and an in-plane magnetic field $B_\parallel$ at $n = 0$, $B_\perp = 0$ and $T = 10$ mK. (e) Two-terminal resistance R as a function of D for different temperatures. The inset shows the size of the activation gap Δ, as determined via Arrhenius fits, as a function of D. (f) Inverse density of states at Fermi level as a function of D for different temperatures calculated from a Hartree-Fock theory for BLG/WSe$_2$ heterostructure at zero level of doping. (g) Trend of the dependence of the correlated gap (direct gap) on the amplitude of the onsite Coulomb interaction $U = U_0 = 1.3\,U_1$ for BLG and proximitized BLG/WSe$_2$ systems. (h) Trend of the dependence of the long-range Coulomb interaction induced spontaneous gap (indirect gap) on the SOC strength λ_I and the dielectric constant ε. The data presented in panels (a), (c)–(e)) was obtained using Device I.

fits (see inset of figure 4(e) and supplementary figure S10). The respective stability of the LAF state in the D, $B_\perp$, $B_\parallel$ space is consistent with the observations made in freestanding graphene, i.e. both states are only stable at low D and become suppressed at finite $D \approx \pm 0.015$ V nm^{-1} (figure 4(a) and supplementary figure S11(a)) and gradually evolve into a CAF at finite $B_\perp$ without apparent changes in the conductance (figure 4(c) and supplementary figure S11(b)). Also the extracted activation gaps are of similar order (see supplementary figure S11(c) for a direct comparison of the gaps). These experimental observations also align with our self-consistent Hartree–Fock calculations addressing both short- and long-range interactions (see methods for details): opening a spontaneous gap in a BLG/WSe$_2$ heterostructure requires a smaller Coulomb interaction (figures 4(f) and (g)), and the larger the induced SOC the stronger the spontaneous indirect gap opening (figure 4(h)). We thus believe that a larger activation gap can be achieved when maximizing the SOC, e.g. by minimizing the twist angle between BLG and WSe_2 [45, 46] or by replacing the WSe_2 with WS_2 [46].

It is worth noting that SOC would introduce single-particle gaps in WSe_2/BLG heterostructures in case they are spin-polarized (figure 4(b)). In this case, the gap would, however, not symmetrically close at finite values of D. Furthermore, the extracted energy gap is approximately one order of magnitude larger than these spin gaps (supplementary figure S17). Lastly, our observations are not only at odds with the single-particle band structure of our WSe_2/BLG heterostructure but also at odds with a previous study of WSe_2/BLG/WSe_2 structures [15, 47], where symmetrically induced Ising SOC results in a single-particle Kane-Mele SOC gap that is suppressed by the application of a $B_{||}$ field [15, 47].

4. Conclusions

In summary, asymmetrically introducing WSe_2 to hBN-encapsulated BLG devices provides a unique platform for the distinct exploration of correlated phases and SOC-induced states, respectively, in the presence of large D fields, depending on the signs of n and D. Whereas a cascade of correlated phases emerges, like those devices without WSe_2, when the charge carriers are polarized on the WSe_2-remote layer of BLG, clear signatures of SOC dominant band splitting have been identified allowing the further measurement of a strong valley g-factor, as if the interaction is nearly absent, when the charge carriers are polarized on the WSe_2-proximate layer of BLG. At zero D field for which the BLG is not layer-polarized, surprisingly, the interaction strength in BLG appears to be enhanced by the induced SOC, giving rise to a correlated insulating state with both theoretically and experimentally anticipated features under $B_\perp$, $B_{||}$, and D fields. Our results have established a rich phase diagram of BLG, paving the way for exploring the interplay between geometry, interaction, and SOC in strongly correlated electrons.

Data availability statement

All data supporting the messages of the manuscript is displayed in the manuscript. The raw data is available from the authors upon request. The data that support the findings of this study are available upon reasonable request from the authors.

Acknowledgments

We thank Michele Masseroni, Thomas Ihn, and Klaus Ensslin for fruitful discussions. R T W and A M S acknowledge funding from the Deutsche Forschungsgemeinschaft (DFG, German Research Foundation) under the SFB 1073 project B10. R T W acknowledges partial funding from the SPP2244 from the Deutsche Forschungsgemeinschaft (DFG, German Research Foundataion). K W and T T acknowledge support from the JSPS KAKENHI (Grant Nos. 20H00354, 21H05233 and 23H02052) and World Premier International Research Center Initiative (WPI), MEXT, Japan. K Z, Y Z and J F were supported by the Deutsche Forschungsgemeinschaft (DFG, German Research Foundation) SFB 1277 (Project No. 314695032), SPP 2244 (Project No. 443416183), the European Union Horizon 2020 Research and Innovation Program under Contract No. 881603 (Graphene Flagship) and FLAGERA project 2DSOTECH. The theoretical work done at UT Dallas was supported by NSF under Grants Nos. DMR-1945351, DMR-2105139, and DMR-2324033. We acknowledge the Texas Advanced Computing Center (TACC) for providing resources that have contributed to the research results reported in this work.

Note from the authors

While analyzing the data we became aware of similar results presented in a manuscript by Masseroni *et al* [48]. It is remarkable that very similar data was obtained by two different groups, using a different TMD on bilayer graphene (WSe_2 in Göttingen and MoS_2 in Zurich).

Author contributions

A.M.S. fabricated Device I and II with help of D.U. and conducted the measurements and data analysis. F.R.G fabricated and measured Device III. K.W. and T.T. grew the hexagonal boron nitride crystals. Y.Z, K.Z, C.Y., J.F. and F.Z. contributed to the theoretical part. All authors discussed and interpreted the data. R.T.W. supervised the experiments and the analysis. The manuscript was prepared by A.M.S., Y.Z., K.Z., J.F., F.Z. and R.T.W. with input from all authors.

Conflict of interest

Authors declare no competing interests.

ORCID iDs

Anna M Seiler https://orcid.org/0000-0002-9883-9220
Klaus Zollner https://orcid.org/0000-0002-6239-3271
David Urbaniak https://orcid.org/0009-0006-4561-1704
Fabian R Geisenhof https://orcid.org/0000-0002-3623-1906
Kenji Watanabe https://orcid.org/0000-0003-3701-8119
R Thomas Weitz https://orcid.org/0000-0001-5404-7355

References

[1] Zhou H *et al* 2021 Half and quarter metals in rhombohedral trilayer graphene *Nature* **598** 429–33

[2] Zhou H, Holleis L, Saito Y, Cohen L, Huynh W, Patterson C L, Yang F, Taniguchi T, Watanabe K and Young A F 2022 Isospin magnetism and spin-polarized superconductivity in Bernal bilayer graphene *Science* **375** 774–8

[3] Zhou H, Xie T, Taniguchi T, Watanabe K and Young A F 2021 Superconductivity in rhombohedral trilayer graphene *Nature* **598** 434–8

[4] Seiler A M, Geisenhof F R, Winterer F, Watanabe K, Taniguchi T, Xie T, Zhang F and Weitz R T 2022 Quantum cascade of correlated phases in trigonally warped bilayer graphene *Nature* **608** 298–302

[5] Seiler A M, Statz M, Weimer I, Jacobsen N, Watanabe K, Taniguchi T, Dong Z, Levitov L S and Weitz R T 2024 Interaction-driven quasi-insulating ground states of gapped electron-doped bilayer graphene *Phys. Rev. Lett.* **133** 66301

[6] Winterer F, Geisenhof F R, Fernandez N, Seiler A M, Zhang F and Weitz R T 2024 Ferroelectric and spontaneous quantum Hall states in intrinsic rhombohedral trilayer graphene *Nat. Phys.* **20** 422–7

[7] Geisenhof F R, Winterer F, Seiler A M, Lenz J, Xu T, Zhang F and Weitz T R 2021 Quantum anomalous Hall octet driven by orbital magnetism in bilayer graphene *Nature* **598** 53–58

[8] Han T, Lu Z, Scuri G, Sung J, Wang J, Han T, Watanabe K, Taniguchi T, Park H and Ju L 2023 Correlated insulator and Chern insulators in pentalayer rhombohedral-stacked graphene *Nat. Nanotechnol.* **91** 181–7

[9] Han T *et al* 2023 Orbital multiferroicity in pentalayer rhombohedral graphene *Nature* **623** 41–47

[10] de La Barrera S C, Aronson S, Zheng Z, Watanabe K, Taniguchi T, Ma Q, Jarillo-Herrero P and Ashoori R 2022 Cascade of isospin phase transitions in Bernal-stacked bilayer graphene at zero magnetic field *Nat. Phys.* **18** 771–5

[11] Holleis L, Patterson C L, Zhang Y, Yoo H M, Zhou H, Taniguchi T, Watanabe K, Nadj-Perge S and Young A F 2023 Ising superconductivity and nematicity in bernal bilayer graphene with strong spin orbit coupling (arXiv: 2303.00742)

[12] Zhang Y, Polski R, Thomson A, Lantagne-Hurtubise É, Lewandowski C, Zhou H, Watanabe K, Taniguchi T, Alicea J and Nadj-Perge S 2023 Enhanced superconductivity in spin–orbit proximitized bilayer graphene *Nature* **613** 268–73

[13] Xie M and Das Sarma S 2023 Flavor symmetry breaking in spin-orbit coupled bilayer graphene *Phys. Rev. B* **107** L201119

[14] Gmitra M and Fabian J 2015 Graphene on transition-metal dichalcogenides: a platform for proximity spin-orbit physics and optospintronics *Phys. Rev. B* **92** 155403

[15] Island J O *et al* 2019 Spin-orbit-driven band inversion in bilayer graphene by the van der Waals proximity effect *Nature* **571** 85–89

[16] Gmitra M and Fabian J 2017 Proximity effects in Bilayer graphene on monolayer $WSe_{\{2\}}$: field-effect spin valley locking, spin-orbit valve, and spin transistor *Phys. Rev. Lett.* **119** 146401

[17] Wang D, Che S, Cao G, Lyu R, Watanabe K, Taniguchi T, Lau C N and Bockrath M 2019 Quantum Hall effect measurement of spin-orbit coupling strengths in ultraclean bilayer graphene/WSe_2 heterostructures *Nano Lett.* **19** 7028–34

[18] Wang Z, Ki D-K, Chen H, Berger H, MacDonald A H and Morpurgo A F 2015 Strong interface-induced spin-orbit interaction in graphene on WS_2 *Nat. Commun.* **6** 8339

[19] Patterson C L *et al* 2024 Superconductivity and spin canting in spin-orbit proximitized rhombohedral trilayer graphene (arxiv:2408.10190)

[20] Li C *et al* 2024 Tunable superconductivity in electron- and hole-doped Bernal bilayer graphene *Nature* **631** 300–6

[21] Koh J M, Thomson A, Alicea J and Lantagne-Hurtubise É 2024 Symmetry-broken metallic orders in spin-orbit-coupled Bernal bilayer graphene *Phys. Rev. B* **110** 245118

[22] Zhang F, Jung J, Fiete G A, Niu Q and MacDonald A H 2011 Spontaneous quantum Hall states in chirally stacked few-layer graphene systems *Phys. Rev. Lett.* **106** 156801

[23] Banszerus L, Möller S, Steiner C, Icking E, Trellenkamp S, Lentz F, Watanabe K, Taniguchi T, Volk C and Stampfer C 2021 Spin-valley coupling in single-electron bilayer graphene quantum dots *Nat. Commun.* **12** 5250

[24] Möller S, Banszerus L, Knothe A, Valerius L, Hecker K, Icking E, Watanabe K, Taniguchi T, Volk C and Stampfer C 2023 Impact of competing energy scales on the shell-filling sequence in elliptic bilayer graphene quantum dots *Phys. Rev. B* **108** 125128

[25] Lee Y *et al* 2020 Tunable valley splitting due to topological orbital magnetic moment in bilayer graphene quantum point contacts *Phys. Rev. Lett.* **124** 126802

[26] Laturia A, van de Put M L and Vandenberghe W G 2018 Dielectric properties of hexagonal boron nitride and transition metal dichalcogenides: from monolayer to bulk *npj 2D Mater. Appl.* **2** 6

[27] Fatemi V and Ruhman J 2018 Synthesizing Coulombic superconductivity in van der Waals bilayers *Phys. Rev. B* **98** 94517

[28] Stepanov P, Das I, Lu X, Fahimniya A, Watanabe K, Taniguchi T, Koppens F H L, Lischner J, Levitov L and Efetov D K 2020 Untying the insulating and superconducting orders in magic-angle graphene *Nature* **583** 375–8

[29] Chuang Y-W, Li J, Fu H, Watanabe K, Taniguchi T and Zhu J 2019 Landau levels of bilayer graphene in a WSe_2/bilayer graphene van der Waals heterostructure *Phys. Rev. B* **100** 195402

[30] Seiler A M, Jacobsen N, Statz M, Fernandez N, Falorsi F, Watanabe K, Taniguchi T, Dong Z, Levitov L S and Weitz R T 2024 Probing the tunable multi-cone band structure in Bernal bilayer graphene *Nat. Commun.* **15** 3133

[31] Icking E *et al* 2022 Transport spectroscopy of ultraclean tunable band gaps in bilayer graphene *Adv. Electron. Mater.* **8** 2200510

[32] Li J, Tan L Z, Zou K, Stabile A A, Seiwell D J, Watanabe K, Taniguchi T, Louie S G and Zhu J 2016 Effective mass in bilayer graphene at low carrier densities: the role of potential disorder and electron-electron interaction *Phys. Rev. B* **94** 161406

[33] Joy S and Skinner B 2023 Wigner crystallization in Bernal bilayer graphene (arXiv: 2310.07751)

[34] Dong Z, Davydova M, Ogunnaike O and Levitov L 2023 Isospin- and momentum-polarized orders in bilayer graphene *Phys. Rev. B* **107** 075108

[35] Lin J-X, Wang Y, Zhang N J, Watanabe K, Taniguchi T, Fu L and Li J I A 2023 Spontaneous momentum polarization and diodicity in Bernal bilayer graphene (arXiv: 2302.04261)

[36] Cheung P, Bao Z and Zhang F 2018 Flavor symmetry and ferroelectric nematics in transition metal dichalcogenides (arxiv:1805.06493)

[37] Freitag F, Trbovic J, Weiss M and Schönenberger C 2012 Spontaneously gapped ground state in suspended bilayer graphene *Phys. Rev. Lett.* **108** 76602

[38] Geisenhof F R, Winterer F, Seiler A M, Lenz J, Zhang F and Weitz R T 2022 Impact of electric field disorder on broken-symmetry states in ultraclean bilayer graphene *Nano Lett.* **22** 7378–85

[39] Velasco J *et al* 2012 Transport spectroscopy of symmetry-broken insulating states in bilayer graphene *Nat. Nanotechnol.* **7** 156–60

[40] Weitz R T, Allen M T, Feldman B E, Martin J and Yacoby A 2010 Broken-symmetry states in doubly gated suspended bilayer graphene *Science* **330** 812–6

[41] Veligura A, van Elferen H J, Tombros N, Maan J C, Zeitler U and van Wees B J 2012 Transport gap in suspended bilayer graphene at zero magnetic field *Phys. Rev. B* **85** 155412

[42] Maher P, Dean C R, Young A F, Taniguchi T, Watanabe K, Shepard K L, Hone J and Kim P 2013 Evidence for a spin phase transition at charge neutrality in bilayer graphene *Nat. Phys.* **9** 154–8

[43] Kharitonov M 2012 Canted antiferromagnetic phase of the $\nu=0$ quantum Hall state in bilayer graphene *Phys. Rev. Lett.* **109** 46803

[44] Zhang F and MacDonald A H 2012 Distinguishing spontaneous quantum Hall states in bilayer graphene *Phys. Rev. Lett.* **108** 186804

[45] Zhang Y *et al* 2024 Twist-programmable superconductivity in spin-orbit coupled bilayer graphene (arxiv:2408.10335)

[46] Li Y and Koshino M 2019 Twist-angle dependence of the proximity spin-orbit coupling in graphene on transition-metal dichalcogenides *Phys. Rev. B* **99** 75438

[47] Kedves M *et al* 2023 Stabilizing the inverted phase of a WSe_2/BLG/WSe_2 heterostructure via hydrostatic pressure *Nano Lett.* **23** 9508–14

[48] Masseroni M *et al* 2024 Spin-orbit proximity in MoS_2/bilayer graphene heterostructures *Nat. Commun.* **15** 9251